Contents lists available at ScienceDirect

Nuclear Inst. and Methods in Physics Research, A

journal homepage: www.elsevier.com/locate/nima

CMOS active pixel sensors response to low energy light ions

E. Spiriti [a,b], Ch. Finck [c,*], J. Baudot [c], C. Divay [d], D. Juliani [c], M. Labalme [d], M. Rousseau [c], S. Salvador [d], M. Vanstalle [c], C. Agodi [e], G. Cuttone [e], M. De Napoli [e], F. Romano [e,f]

[a] *Istituto Nazionale di Fisica Nucleare-Laboratori Nazionali di Frascati, Italy*
[b] *Istituto Nazionale di Fisica Nucleare-Sezione di Roma 3, Italy*
[c] *Université de Strasbourg, CNRS, IPHC UMR 7871, F-67000 STRASBOURG, France*
[d] *LPC-Caen, ENSICAEN, Université de Caen, CNRS/IN2P3, Caen, France*
[e] *Istituto Nazionale di Fisica Nucleare-Laboratori Nazionali del Sud, Italy*
[f] *Centro Studi e Ricerche e Museo Storico della Fisica "Enrico Fermi", Roma, Italy*

ARTICLE INFO

ABSTRACT

Recently CMOS active pixel sensors have been used in Hadrontherapy ions fragmentation cross section measurements. Their main goal is to reconstruct tracks generated by the non interacting primary ions or by the produced fragments. In this framework the sensors, unexpectedly, demonstrated the possibility to obtain also some informations that could contribute to the ion type identification. The present analysis shows a clear dependency in charge and number of pixels per cluster (pixels with a collected amount of charge above a given threshold) with both fragment atomic number Z and energy loss in the sensor. This information, in the FIRST (**F**ragmentation of **I**ons **R**elevant for **S**pace and **T**herapy) experiment, has been used in the overall particle identification analysis algorithm. The aim of this paper is to present the data analysis and the obtained results. An empirical model was developed, in this paper, that reproduce the cluster size as function of the deposited energy in the sensor.

1. Introduction

The understanding of the underlying processes in nuclear fragmentations has risen in interest in the last decade especially for space [1,2] and hadrontherapy [3,4] applications. Monte Carlo simulations [5,6] with various theoretical models for the fragmentation process differ up to an order of magnitude, compared to experimental data, for double-differential quantities (e.g. in energy and in angle) [7–9]. The FIRST experiment measured differential fragmentation cross-sections of carbon beam with an energy ranging from 400 to 1000 MeV/u in energy on different material [10]. In this experiment, designed as a Time-Of-Flight (TOF) mass spectrometer, the position of the emission point (i.e., the vertex) of secondary charged particles produced by the carbon ion fragmentation was determined using a tracking system based on a thin pixelized silicon Complementary Metal Oxide Semi-conductor (CMOS) detector. In such experiments, the particle identification is a key ingredient to properly separate all fragment species.

The aim of this paper is to quantify how much information could be extracted from the CMOS trackers with respect to the particle identification. For this purpose, three different measurement campaigns were achieved, using either digital output CMOS detectors Mimosa26 (M26) [11] or analog output CMOS detectors Mimosa18 (M18) [12]. The first data taking campaign was motivated by the characterization of the M26 sensor under beam conditions with the FIRST experiment vertex detector, the second was the experiment itself data collection. The last one was specifically scheduled to verify the possibility to extract specific informations from the monolithic pixel sensors about the low energy light ions particle identification. For this purpose a specific $\Delta E - E_{tot}$ telescope [8], as a reference detector to independently identify the ion type and energy, was used. In this campaign, the analogical sensor M18 was used specifically to measure the collected charge contrary to what could be done with a digital one as M26 sensor. Then, on this basis, the response of the pixel sensors has been evaluated.

2. Mimosa 26 and Mimosa 18 description

In this section, the main properties of the M26 and M18 chips are presented.

2.1. M26 chip

The M26 CMOS sensor has an epitaxial layer thickness of 14 μm and an overall thickness of 50 μm. The sensor has a sensitive area of 10.6 × 21.2 mm^2 subdivided in 576 rows and 1152 columns of pixels with 18.4 μm pitch. In-pixel amplification and double sampling generated the signal sent to the bottom of the matrix where are discriminated by one comparator per column. The entire matrix is read out within 115.2 μs in a parallel column rolling shutter mode. A pixel in the M26 sensor is considered as fired when the collected charge is above a common threshold, unlike analogical sensors [13] where the amplitude of the signal is also provided. Four thresholds, each of them common to one fourth of the matrix, were adjusted to reduce the number of fake pixels and maintain a high detection efficiency. For our study, the thresholds were set at 5 σ level above the pedestal. All the digital signals produced by the M26 sensors were collected with two CAEN V1495 VME boards [14]. A specific JTAG control software to initialize the M26 sensors through the VME V1495 interface was implemented.

2.2. M18 chip

The M18 chip, contrary to the M26 chip, has an analog output and do not include in-pixel double sampling capability. The sensor active area of 5.1 × 5.1 mm^2 is segmented in 512 rows and 512 columns of pixels with a 10 μm pitch. The epitaxial layer and overall thickness are the same as for the M26 chip. The readout of the M18 chips relies on a sequential steering from pixel to pixel and is subdivided into four sub-matrices. The signals from the two M18 sensors, 4 differential analog signal for each of the four sub-matrix, were digitized by the VME board SIS3301 from Struck company [15]. The signals were sampled at 20 MHz frequency with an overall time of 6.5536 ms to sample twice the entire sub-matrix of 256 × 256 pixels. The two samples of each pixel were subtracted and then compared to a predefined pedestal value, in order to store on disk only the signal pixel values above a given threshold. As for the M26 chips the thresholds were set at 5 σ level above the pedestal.

3. Experimental setups

During three different campaigns, the number of pixels and/or the charge in a sensor were measured, for each impinging ions, as a function of the atomic number Z and, when possible, as function of the energies of the detected particles.

The first campaign was performed at the INFN-Catania Superconducting Cyclotron with proton and carbon ion beam with an energy of 80 MeV/u using the vertex detector based on M26 chips in the FIRST configuration. The data of the second campaign were a subset of the one collected during the FIRST experiment at GSI with impinging carbons of 400 MeV/u onto an 8 mm thick composite target [10]. The particle identification was done with a Time-Of-Flight technique. The eight M26 chips used during the first and second campaigns were assembled in the same way as for the FIRST experiment. The tracker was constituted of 4 planes, each plane composed by two M26 chips leading to a sensitive area of 2.12 × 2.12 cm^2 with an overlapping region of ∼100 μm in X direction. The distance of two consecutive planes was 3 mm, producing an overall thickness of the four vertex planes of 12 mm.

The setup for the third campaign consisted of two M18 sensors, separated by 1.6 mm. A $\Delta E - E_{tot}$ telescope was located at ∼40 cm behind the M18 sensors. Data were collected at Catania accelerator at 80 MeV/u impinging carbon onto a 13.3 mm thick PMMA target. The ΔE part of the telescope was a (487 ± 13) μm thick silicon detector. The diameter of this detector was 22 mm. The total energy E_{tot} was measured thanks to a conical shaped CsI scintillator, with a length of 75 mm, coupled to a photomultiplier. A collimator with 4 mm radius and 5 cm length between the target and the silicon detectors allowed to select the angle of the detected fragments. The collimator was placed at

Table 1
Spatial resolutions σ_X and σ_Y in X and Y direction at 80 and 400 MeV/u of ^{12}C beam using M26 sensors. The corresponding proportion of tails (events outside the window of $\pm 4\sigma$) in X and Y direction are addressed in fourth and fifth columns. The last one stands for the number of reconstructed tracks used to produced the residual distributions.

Energy (MeV/u)	σ_X (μm)	σ_Y (μm)	Tail$_X$ (%)	Tail$_Y$ (%)	Number of tracks
80	3.44 ± 0.01	2.23 ± 0.01	9.8	8.4	2130
400	6.00 ± 0.01	4.47 ± 0.01	14.2	14.7	3500

an angle of 3° respect to the beam axis. This setup was implemented to take care to the unavailability of beams for all ion species up to $Z = 6$. The used PMMA target had a thickness slightly larger then the Bragg peak position in this material with the specific energy of the impinging carbon ions beam used. The collimator and the tracker itself were used to select single track while the telescope to identify the ion species. A specific Monte Carlo simulation of the setup itself was, on purpose, implemented to evaluate the obtainable rate in those conditions.

4. Analysis software design

The reconstruction software for data analysis was based on the one used in the framework of the FIRST package [16]. The fired pixels of the vertex detector were extracted from the raw data files, for each sensor, a clustering algorithm was used to reconstruct the crossing point of the ionizing particle through the M26/M18 sensors. Tracking reconstruction was based on standard algorithms tuned for the specific applications of the CMOS sensors. The efficiency of clustering and tracking was higher than 98% [16]. The residuals are defined as the distance between the cluster position and the position of the intercept of the reconstructed track in the different planes [16]. The alignment procedure was the one developed for the FIRST package [10] consisting of the minimization of the residuals with the displacement of the planes in X and Y direction and the rotation of planes around the Z axis.

Fig. 1 shows the residuals obtained with carbon ions tracks at 80 MeV/u and 400 MeV/u for the X and Y coordinates using the FIRST geometry of the vertex detector. The distributions were normalized for better comparison. The spatial resolution of the tracking device (σ), extracted from a Gaussian fit applied onto the residual distributions, and the corresponding errors are listed in Table 1 as well as the proportion of events in the tail and the number of used tracks. The proportion of events outside the range of $\pm 4\sigma$ was defined as tail. A resolution better than 6 μm in X and Y direction and a tail population of the distributions less than 15% was obtained, regardless the energy of the carbon beam. The poorer resolution in X direction was due to the geometry as described in Section 3. Indeed, in X direction, each sensor had to be aligned respect to the other sensor in the same plane. The difference in resolution reflected the corresponding alignment errors.

5. Data analysis for M26 sensors

5.1. Cluster size distributions

In Table 2 are reported the mean and RMS values of distribution computed from the cluster size (i.e., the number of pixels per cluster) distributions for proton and carbon ions at the two different energies of 80 MeV/u (data collected during the first campaign) and 400 MeV/u (data collected during the second campaign). A clear dependency of the cluster size versus the ion type and energy was observed (see Table 2).

For example, the mean and RMS value of the cluster size for protons at 80 MeV was (4.3 ± 1.7) compared to (21.1 ± 4.7) for carbon ions at the same energy. Although carbon ions lose 40 times more energy than protons [17] in the sensor, the mean value for the carbon ion cluster size distribution was only a factor ∼5 higher than the one of the proton distribution. The cluster size was not linearly related to the energy loss.
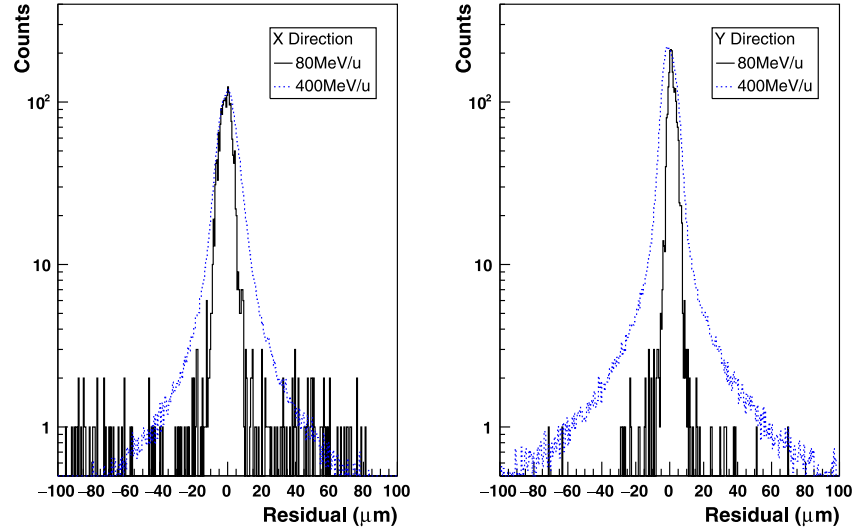
Fig. 1. Residuals obtained for reconstructed tracks originated from 80 MeV/u and 400 MeV/u carbon beams using the M26 sensors. The two plots have the same binning and were normalized at the maximum value for comparison.

Table 2
Mean value ($\langle size \rangle$) and corresponding standard deviation value ($RMS_{\langle size \rangle}$) of the cluster size distribution for proton and carbon ion beams at 80 MeV/u and 400 MeV/u using the M26 sensors. The last column indicates the number of reconstructed clusters.

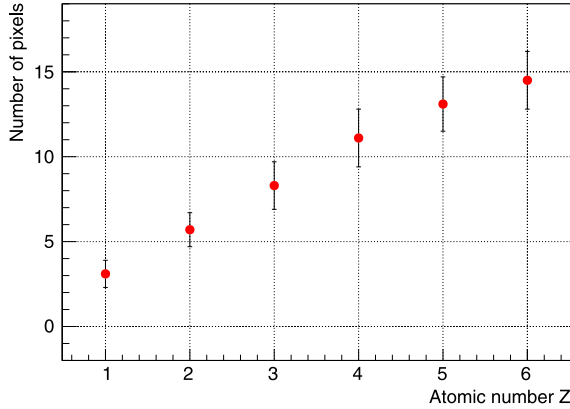| Ion	Energy (MeV/u)	$\langle size \rangle$	$RMS_{\langle size \rangle}$	Number of clusters
p	80	4.3	1.7	3800
^{12}C	80	21.1	4.7	6300
^{12}C	400	14.7	1.9	369 000

Fig. 2. Cluster size distribution using M26 sensors as a function of the atomic number Z of the emitted fragments at 400 MeV/u energy after 8 mm target.

Furthermore, the spread (i.e., the RMS of the distribution) and mean value of the cluster size was larger for carbon ions at an energy of 80 MeV/u (21.1 ± 4.7) than at the energy of 400 MeV/u (14.7 ± 1.9). This difference is clearly related to higher energy loss for lower carbon ion energy.

5.2. Fragment atomic number dependency

Fig. 2 presents the cluster size as a function of the atomic number Z of the fragments outgoing from the target for the 400 MeV/u data collected during the second campaign. The different Z particles were selected using a selection algorithm on the FIRST data, mainly from the TOF detector [10] placed after the magnetic field, and fitting each of the cluster size distribution with a Gaussian. The error bars corresponded to the σ value of the Gaussian fit. A clear dependence was visible even
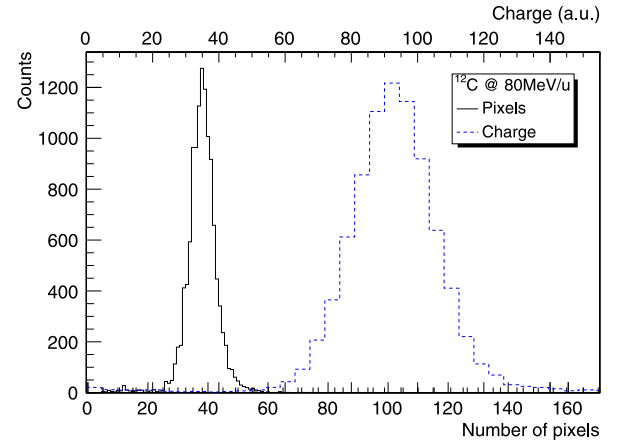

Fig. 3. Number of pixels per cluster distribution (solid line) with the associated charge (dashed line) for carbon ions at 80 MeV/u using M18 sensors. The data were taken with the beam directly impinging on the sensors.

though it was not sufficient to completely disentangle all fragment types. Indeed for particles with $Z \geq 3$, the cluster size distributions started to overlap as shown by the error bars.

6. Data analysis for M18 sensors

The results, presented in this section, were obtained with data collected during the third campaign using the analogical output M18 sensors.

6.1. Cluster size and charge distributions

Fig. 3 shows the cluster size and the associated collected charge for carbon ions at 80 MeV/u. The carbon ions impinging directly onto the sensors. To avoid pileup events in the sensor as well as in the telescope, events with only one reconstructed track were selected. With (38.0 ± 5.3) pixels per cluster, the number of fired pixels was nearly twice as large compared to the cluster size distribution of the M26 sensors with (21.1 ± 4.7) pixels per cluster. Since the epitaxial layer was the same for both detectors, the difference was ascribed to the pixels pitch, 18 μm and 10 μm for M26 and M18 chip, respectively.
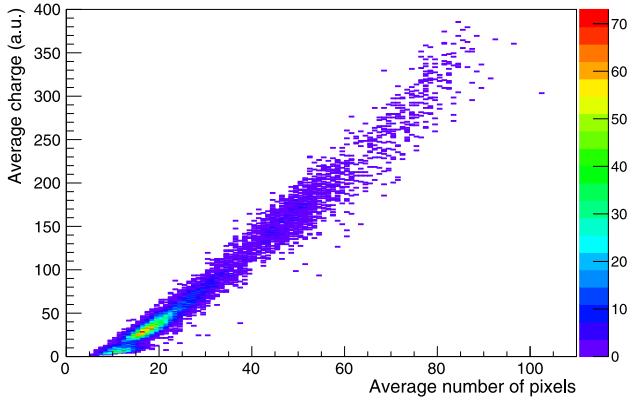
Fig. 4. Average charge per cluster versus the number of pixels per cluster for carbon ions at 80 MeV/u impinging the PMMA target using M18 sensors.
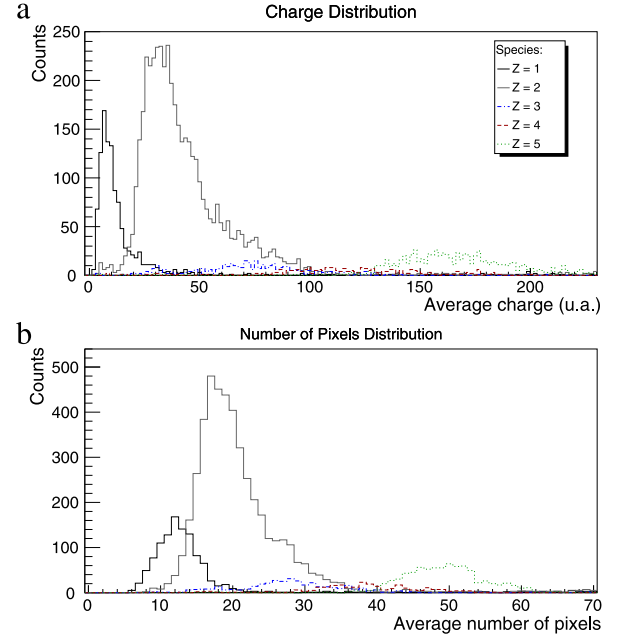

Fig. 6. Average charge distribution (a) and average number of pixels per cluster (b) using M18 sensors for fragments with atomic number $Z = 1$–5, selected with the telescope (for the full color figures, the reader is referred to the web version of this article).

Fig. 4 shows a clear correlation between the charge per cluster for M18 sensors and the associated cluster size for the run corresponding to fragments coming from carbon ions onto the PMMA target reaction at 80 MeV/u. The delta electrons originated from the collimator and hitting the first sensor were removed by applying a threshold on the charge distribution of the first sensor versus the charge of second sensor. After applying this cut, the correlation factor between the average charge of the two sensors and the cluster size was higher than 98%.

The selection of fragment species and energy was performed thanks to the telescope. The different species were selected using cuts on the two dimensional plot of the energy loss in the silicon detector versus the CsI scintillator charge following the KaliVeda method described in [18]. This selection grid obtained with that method is depicted in Fig. 5(a). The main advantage of this method was to perform both detector calibration and particle identification simultaneously. A typical calibrated identification map in energy is shown in Fig. 5(b).

Fig. 6(a) shows the average charge distribution of sensor 1 and 2 for fragments with atomic number from $Z = 1$ to $Z = 5$. The atomic number of the fragments were selected by using the KaliVeda grid onto two dimensional plot of the energy loss in the silicon detector versus the CsI scintillator deposited charge ($\Delta E - E_{tot}$ map) for the carbon ions impinging the PMMA target data. The most produced fragments were the ones with atomic number $Z = 1$ and 2.

Table 3 summarizes the mean values and the corresponding standard deviations (RMS) for the average charge and cluster size distributions versus the atomic number of the detected fragments. The values of the average charge follows a quadratic law with the atomic number Z as expected by the Bethe-Bloch formula. However for higher Z ($Z \geq 4$), the average charge starts to deviate from this law.

Table 3

Mean value $\langle charge \rangle$ and corresponding RMS $RMS_{\langle charge \rangle}$ for the average charge distributions as function of the atomic number (Z) of the emitted fragments for carbon at 80 MeV/u on a 13.3 mm PMMA target using the M18 sensors. Also reported are the values, $\langle size \rangle$ and $RMS_{\langle size \rangle}$, for the cluster size distributions.

Z	$\langle charge \rangle$	$RMS_{\langle charge \rangle}$	$\langle size \rangle$	$RMS_{\langle size \rangle}$
1	9.1	3.8	12.1	2.1
2	39.8	12.3	19.3	3.6
3	79.3	16.8	29.2	4.5
4	114.5	18.4	38.1	5.1
5	160.0	16.9	47.0	4.2

6.2. Fragment atomic number dependence

The fragment species identification was performed with the telescope. The data were taken with carbon ions impinging onto the PMMA target. The charge distribution, measured with the M18 sensors, was plotted for the different fragment species, in order to evaluate the separation power of these sensors (see Fig. 6(a)). The efficiency $\varepsilon_Z(chg)$ as a function of the applied window on the M18 charge (chg)
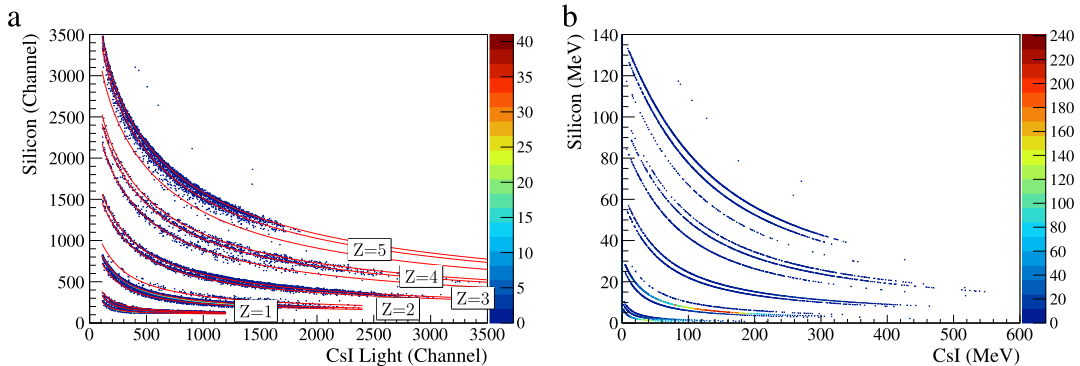

Fig. 5. The $\Delta E - E_{tot}$ map: energy loss in the silicon detector versus the total energy measured with the CsI scintillator, with the KaliVeda calibration (a) and the ΔE–E map calibrated in energy (b) (for the full color figures, the reader is referred to the web version of this article).

Table 4
Purity $\mathcal{P}_Z$ and efficiency $\mathcal{E}_Z$ for applied cuts on the M18 average charge distribution to select the atomic number (Z) of the emitted fragments.

Z	Cut selection	$\mathcal{P}_Z$ (%)	$\mathcal{E}_Z$ (%)
1	[4, 16]	92 ± 1	69 ± 2
2	[20 ,56]	93 ± 1	75 ± 1
3	[64, 136]	23 ± 3	62 ± 3
4	[82, 154]	26 ± 3	78 ± 3
5	[128, 204]	81 ± 1	86 ± 1

distribution was defined as follows :

$$\mathcal{E}_Z(chg) = \frac{N(chg)}{N(Z)} \tag{1}$$

where $N(chg)$ was the number of events selected when applying a window on the M18 charge distribution and $N(Z)$ was the number of events selected with KaliVeda method for a given atomic number Z. The purity $\mathcal{P}_Z(chg)$ was defined as the efficiency:

$$\mathcal{P}_Z(chg) = \frac{N_Z(chg)}{N(Z)} \tag{2}$$

but considering only the events $N_Z(chg)$ corresponding to the selection of the given atomic number Z in $\Delta E - E_{tot}$ map. Thus the purity $\mathcal{P}_Z(chg)$ reflected the proportion of events that were well identified in Z for a given cut in the M18 charge distribution. The windows on the charge distribution were chosen to maximize both purity and efficiency.

Table 4 summarizes the results obtained for purity $\mathcal{P}_Z(chg)$ and efficiency $\mathcal{E}_Z(chg)$ with their associated errors for each charge Z of the emitted fragment. As expected the best result was obtained for $Z = 2$ since the α and ^{3}He particles were the mostly produced fragments. Indeed the purity was 93 ± 1% with an associated efficiency of 75 ± 1%. The protons were contaminated in the charge distribution of α-like fragments, therefore the purity was slightly smaller with a value of 92 ± 1% keeping an efficiency of 69 ± 2%. Nevertheless it was possible to separate these two fragment species. The fragments with atomic number Z ≥ 3 exhibited broader charge distributions (see Fig. 6(a)) since their total energy distributions were larger than for $Z = 1$ or $Z = 2$. Consequently the purity was low, lower than 30%, with an efficiency still higher than 60%. In that case, an accurate selection for this fragment with the M18 sensor was not possible. Fragments with $Z = 5$ presented a better situation since the distribution was well separated from the other charge distributions even though its distribution was as large as for the $Z = 3$ and $Z = 4$. Indeed the purity was 81 ± 1% with an efficiency close to 90%. Fragments with atomic number higher than $Z = 3$ and $Z = 4$ suffered also from their low production rate.

Fig. 6(b) shows the average number of pixels per cluster as a function of the fragment atomic number of the emitted fragments. The cluster size distributions were less separated, leading to smaller purities. Indeed, except for the atomic charge $Z = 2$, the purity values dropped by a factor of 3–4 compared to selection performed on the average charge distributions. Even for $Z = 1$, the purity was smaller by 30% . Therefore using the number of pixels per cluster for atomic charge selection was less efficient than with the average charge distributions.

6.3. Energy dependency for fragments with atomic number Z = 2

Only results for fragments with atomic number $Z = 2$ were considered. For higher Z fragments, the statistic was too low, whereas for fragment with $Z = 1$, the spread in total kinetic energy was too small to see any effect in the charge distribution of the sensor.

For $Z = 2$ fragments, the average charge measured with M18 sensors is plotted as a function of the total energy in Fig. 7. A fit was performed with a $\log(x)/x$ function, taking into account the behavior of the Bethe-Bloch formula with the kinetic energy at small energies. The higher the energy, the lower the deposited energy in the sensor and therefore the lower the charge value. Although the charge distributions were large, a rough estimation of the energy for $Z = 2$ fragments could be performed. Indeed the total energy could only be selected with a bin of ~30 MeV of the average charge.
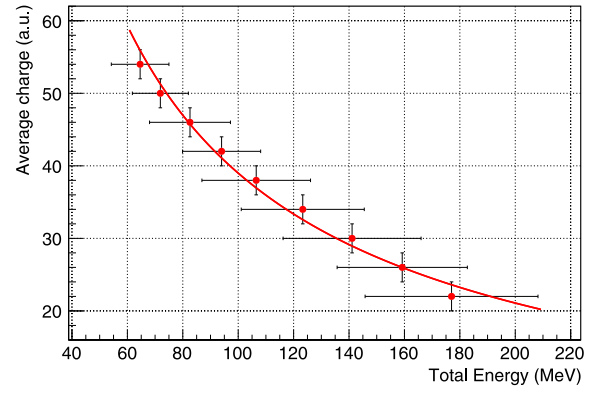

Fig. 7. Total energy mean value and associated standard deviation (RMS) measured with the telescope versus the average number of charge collected in the M18 sensors. The red line corresponds to a fit with the logarithm function $\log(x)/x$. These results were obtained for fragments with atomic number $Z = 2$.
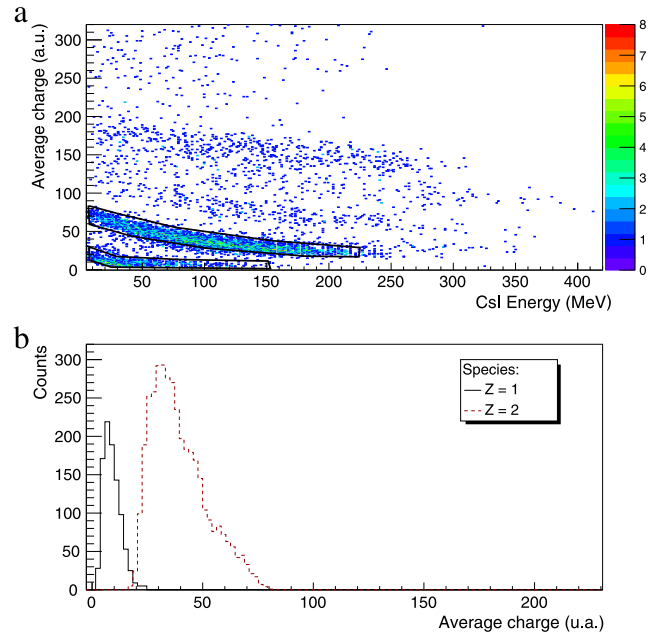

Fig. 8. Average charge measured with the M18 sensors versus the energy of the CsI scintillator with the associated graphical cuts for $Z = 1$ and $Z = 2$ (a) used to obtain average charge distribution for $Z = 1$ and $Z = 2$ fragments (b).

6.4. Identification map with M18 sensors

In this section the ΔE silicium detector of the telescope, was replaced by the M18 sensors. The goal was to quantify the particle identification resolution with a 14 μm thick sensor. The $\Delta E - E_{tot}$ identification map built with the M18 sensor as ΔE detector is shown in Fig. 8(a). In that case, the average charge measured in the M18 sensors versus the scintillator energy was used. The line corresponding to fragments with atomic number $Z = 1$ and $Z = 2$ can clearly be identified. The deposited energy in the sensors was small, since the small thickness of the active area. Graphical cuts around the $Z = 1$ and $Z = 2$ lines were drawn as shown in Fig. 8(a). The projection of the average charge for the given cuts is shown in Fig. 8(b). Compared to Fig. 6(a), the two distributions were well separated and the purity was close to 99% in this case. So in that case the particle identification was possible for fragments with atomic number $Z = 1$ and $Z = 2$. For higher Z, the lack of statistics prevented to conclude.
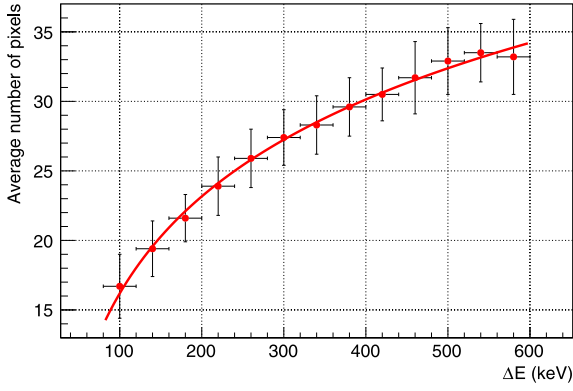
Fig. 9. Average number of pixels per cluster and associated RMS versus the computed energy loss ΔE in the M18 sensor. The red line corresponds to the fit obtained with our model. These results were obtained for fragments with atomic number $Z = 2$.

7. Empirical cluster size model

The cluster size was measured, with the M18 sensors, for fragments with atomic number $Z = 2$. These data were collected during the third campaign with the carbon ions impinging to the PMMA target. From the total energy, measured with the CsI scintillator, the deposited energy ΔE in the 14 μm silicon was computed. The stopping power tables of α particles in silicon were taken from ICRU49 [19]. The cluster size as a function of the energy loss in the sensor is shown in Fig. 9. Neglecting any space charge effect in the sensor, the charge density over a given area $dq(r)/dS$, where r is the radial distance to the impact point, could be roughly described by a Gaussian shape:

$$\frac{dq(r)}{dS} = \frac{Q_{tot}}{2\pi\sigma^2} exp\left(-\frac{r^2}{2\sigma^2}\right)$$

where σ is the spread of the distribution, $Q_{tot} = \Delta E / E_g$ is the total charge deposited in the sensor and E_g is the mean energy for the creation of charge carriers, for silicon material $E_g = 3.6 \times 10^{-3}$ keV. A pixel is fired when the collected charge is higher than a given threshold T:

$$\frac{dq(r_T)}{dS} = T \quad \text{hence} \quad r_T = 2\sigma^2 Log\left(\frac{\Delta E}{2\pi E_g T \sigma^2}\right)$$

where r_T is the distance to the impact beyond which pixels will not be fired anymore. Assuming a radial distribution of the charge over the pixels, the number of pixels n_p, as a function of the energy loss ΔE, could be written as:

$$n_p = \frac{\pi r_T^2}{p^2} = 2\pi r_s Log\left(\frac{\Delta E}{2\pi E_g T_s}\right) \quad (3)$$

where p is the size of a pixels. The parameters $r_s = \sigma^2/p^2$ and $T_s = T\sigma^2$ are the two free parameters of the model. In Fig. 9, the experimental data were fitted with Eq. (3). Our simplistic model reproduced well the data. Since the cluster size did not depend linearly on ΔE values, this led to a poorer selection capability, especially for high values of ΔE (i.e., low kinetic energy fragments). This non-linear behavior effect of

cluster size with the charge produced in silicon layer was also observed with the M26 sensors (see Section 5.1).

8. Conclusions

In the paper, the response function of two different CMOS sensors, namely M26 and M18, was investigated for low energy fragments. Even for the digital output sensor (M26), a clear dependance was shown on the cluster size as function of the fragment atomic number (Z). It was possible with a one σ cut on the cluster size distribution to perform a selection for fragment species with $Z = 1$ up to $Z = 3$. For M18 sensors, providing appropriate cuts on the charge distributions, it was possible to select fragment species $Z = 1, 2$ and $Z = 5$ with a high efficiency and high purity, greater than 80% and greater than 69% respectively. For $Z = 3$ and $Z = 4$, the efficiency was still correct (>62%) but with a deteriorated purity (< 30%). A clear dependance of the M18 charge as a function of the fragment kinetic energy with $Z = 2$ was shown. Using M18 as a ΔE detector combined with a CsI scintillator as E_{tot} detector, led to purity higher than 99% for the separation of fragment for $Z = 1$ and $Z = 2$. Using CMOS sensor could strongly help in particle charge identification for $Z = 1$ up to $Z = 3$ even with a digital output. An empirical model, described in the paper, was able to reproduce the cluster size as function of the deposited energy in the M18 sensor.

References

[1] M. Durante, F.A. Cucinotta, Rev. Modern Phys. 83 (2011) 1245.
[2] L. Ziwei, Phys. Rev. C 75 (2007) 034609.
[3] D. Schardt, T. Elsasser, D. Schulz-Ertner, Rev. Modern Phys. 82 (2010) 383.
[4] J.S. Loeer, M. Durante, Nat. Rev. Clin. Oncol. 10 (2013) 411.
[5] K. Parodi, S. Brons, F. Cerutti, A. Ferrari, A. Mairani, H. Paganetti, F. Sommerer, Proc. 12th Int. Conf. on Nucl. Reac. Mechan., 2009.
[6] T.T. Böhlen, et al., Phys. Med. Biol. 55 (2010) 5833.
[7] J.H. Heinbockel, et al., Adv. Space Res. 47 (2011) 1079.
[8] J. Dudouet, et al., Phys. Rev. C 88 (2013) 024606.
[9] J. Dudouet, et al., Phys. Rev. C 89 (2014) 054616.
[10] M. Toppi, et al., Phys. Rev. C 93 (2016) 064601.
[11] Ch. Hu-Guo, et al., Nucl. Instrum. Methods Phys. Res. A 623 (2010) 480.
[12] W. Dulinski, et al., Conference records of the IEEE Nuclear Science Symposium, 2007, p. 4437182.
[13] G. Deptuch, et al., Nucl. Instrum. Methods Phys. Res. A 512 (2003) 299.
[14] http://www.caen.it/nuclear/product.php?mod=V1495.
[15] http://www.struck.de.
[16] R. Rescigno, et al., Nucl. Instrum. Methods Phys. Res. A 767 (2014) 34.
[17] E. Spiriti, M. De Napoli, F. Romano, et al., Nuclear Phys. B Proc. Suppl. 215 (2011) 157.
[18] J. Dudouet, et al., Nucl. Instrum. Methods Phys. Res. A 715 (2013) 98.
[19] H.O. Wyckoff, et al., Int. Comm. Radiat. Units Meas. 49 (1993).